Materials Research Express

PAPER

RECEIVED
18 July 2016

REVISED
28 September 2016

ACCEPTED FOR PUBLICATION
5 October 2016

PUBLISHED
24 October 2016

A statistical model for the wettability of surfaces with heterogeneous pore geometries

Lance Brockway[1,2] **and Hayden Taylor**[1,2]

[1] Department of Mechanical Engineering, 6159 Etcheverry Hall, University of California, Berkeley, CA 94720, USA
[2] Berkeley Education Alliance for Research in Singapore (BEARS) CREATE Tower, 1 Create Way, #11-00 Singapore 138602

E-mail: hkt@berkeley.edu

Keywords: superhydrophobic, omniphobic, porous, nanostructure, contact angle, reentrant

Abstract

We describe a new approach to modeling the wetting behavior of micro- and nano-textured surfaces with varying degrees of geometrical heterogeneity. Surfaces are modeled as pore arrays with a Gaussian distribution of sidewall reentrant angles and a characteristic wall roughness. Unlike conventional wettability models, our model considers the *fraction* of a surface's pores that are filled at any time, allowing us to capture more subtle dependences of a liquid's apparent contact angle on its surface tension. The model has four fitting parameters and is calibrated for a particular surface by measuring the apparent contact angles between the surface and at least four probe liquids. We have calibrated the model for three heterogeneous nanoporous surfaces that we have fabricated: a hydrothermally grown zinc oxide, a film of polyvinylidene fluoride (PVDF) microspheres formed by spinodal decomposition, and a polytetrafluoroethylene (PTFE) film with pores defined by sacrificial polystyrene microspheres. These three surfaces show markedly different dependences of a liquid's apparent contact angle on the liquid's surface tension, and the results can be explained by considering geometric variability. The highly variable PTFE pores yield the most gradual variation of apparent contact angle with probe liquid surface tension. The PVDF microspheres are more regular in diameter and, although connected in an irregular manner, result in a much sharper transition from non-wetting to wetting behavior as surface tension reduces. We also demonstrate, by terminating porous zinc oxide with three alternative hydrophobic molecules, that a single geometrical model can capture a structure's wetting behavior for multiple surface chemistries and liquids. Finally, we contrast our results with those from a highly regular, lithographically-produced structure which shows an extremely sharp dependence of wettability on surface tension. This new model could be valuable in designing and evaluating processes for manufacturing liquid-repellent surfaces on an industrial scale.

Introduction

It has been well established that tuning a surface's micro- and nano-structure can greatly increase the apparent contact angle of a liquid on the surface, rendering it superhydrophobic or superoleophobic [1–3]. One important way in which the apparent contact angle, and hence liquid repellence, can be increased is by reducing the fraction of a liquid's surface that comes into contact with solid material—a relationship that was first modeled by Cassie and Baxter [4]. The aim of reducing contact area can be achieved by patterning a surface with micro- and nano-scale pillars or porous structures that support the liquid. Giving these surface features a re-entrant or under-cut shape where they meet the liquid ($\Psi > 90°$ in figure 1(c)) is particularly valuable, because this directs the surface tension of the liquid out of the pores and enables the surface to repel the liquid, even including low-surface-tension oils and fluorinated liquids that will wet almost any smooth surface. When re-entrant features are combined with a low-surface-energy termination, such as a fluorinated molecule, the repellence is further enhanced.

There have been many experimental studies of how re-entrant geometries can impart high liquid-repellence to a surface. Geometrically highly regular hydrophobic and oleophobic surfaces have been made

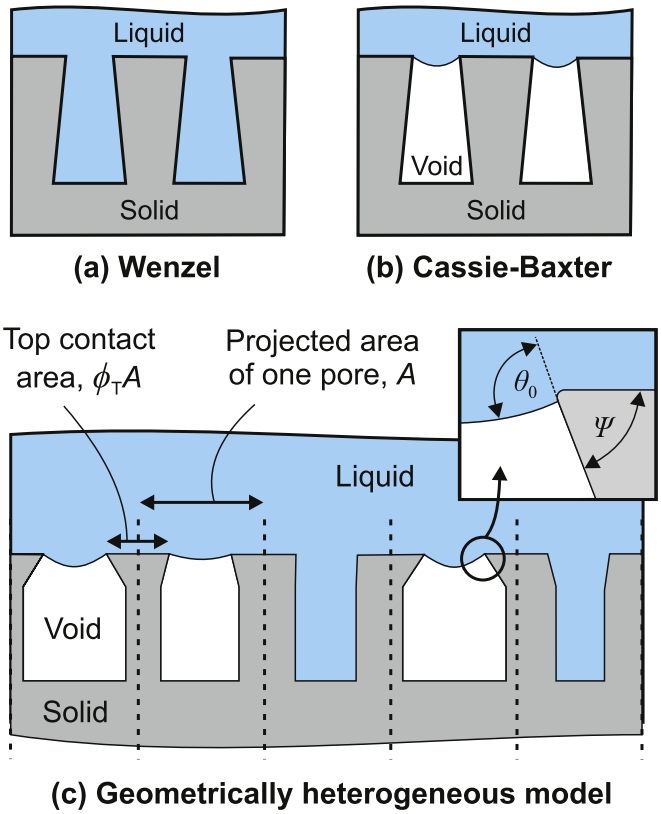

Figure 1. Pore geometry and the effect of its variability on a liquid's apparent contact angle. The classical (a) Wenzel and (b) Cassie–Baxter models assume completely spatially uniform surface feature geometries with a fixed re-entrant angle $\boldsymbol{\Psi}$, resulting in complete wetting (a) where $\boldsymbol{\theta}_0 < \boldsymbol{\Psi}$ or complete non-wetting (b) where $\boldsymbol{\theta}_0 > \boldsymbol{\Psi}$. Real surfaces exhibit a *range* of effective $\boldsymbol{\Psi}$, such that the *fraction* of pores filled will depend on θ_0 (c).

lithographically. The microfabrication of re-entrant structures with this purpose was originally demonstrated by Tuteja, who patterned and etched SiO_2 disks on a silicon substrate, and then under-cut the disks with an isotropic silicon etch [1]. After vapor-phase silanization, these structures were shown to deliver advancing contact angles in excess of 160° with octane. Liu subsequently extended this approach with doubly-reentrant structures that were formed by a multi-stage oxidation and etching process [5]. These structures offer re-entrant angles Ψ in excess of 180° and apparent contact angles above 150° even for liquids with surface tension as low as 10 mN m^{-1}.

Although precisely fabricated, highly regular geometries have provided deeper understanding of how to engineer a liquid-repellent surface, many of the potential applications require large, non-flat surfaces to be modified at low cost [6]. The most lucrative of these applications include waterproof and stain-resistant clothing [7–9], food packaging and processing equipment [10], filters for separating oil and water [1, 11], anti-icing coatings for aircraft [12, 13], drag reduction in transport [14], antimicrobial coatings [15, 16], and the enhancement of heat-transfer by promoting dropwise condensation [17–19]. What these applications have in common is a requirement to augment pre-existing materials and geometries with the micro- and nano-structures that will enhance liquid repellence. Standard microfabrication techniques, including photolithography and plasma etching, have limited applicability in these situations since the techniques may require highly polished target surfaces, vacuum processing, and the use of specialized etchant gases.

Traditional manufacturing processes—including stamping, embossing, injection or compression molding, or knurling—may have a role to play in delivering affordable liquid-repellent surfaces. However, re-entrant features are more challenging to manufacture at scale than, for example, simple vertical pillar arrays, because almost any mechanical process for imparting surface texture involves pressing the target material against a tool and then separating them, and so is not capable of creating re-entrant geometries.

Consequently, bottom-up fabrication processes have been widely explored. Prominent among them has been the controlled oxidation of metal surfaces and the precipitation of oxides and hydroxides to create porous films of, for example, anodic alumina [20–22], copper oxide [17, 18], zinc oxide [23–25], and brucite-type cobalt hydroxide [26]. The morphologies of grown and precipitated structures have ranged from porous films [20–22] to stacks of needles with deep sub-micron tip radii [17, 18, 26]. These structures are all irregular in shape and,

with the exception of anodic alumina, contain many re-entrant features. Ceramic surfaces are particularly suited to heat-transfer applications because they can be applied directly to a metallic component, the coatings themselves are much more thermally conductive than polymeric materials, and they can be grown in films less than a micrometer thick.

The ability to grow an oxide on to any shape of surface has enabled these structures to be combined with pre-textured surfaces such as woven metal meshes [27]. The oxide nanostructures together with the sub-millimeter features of the woven mesh yields structures with at least two length-scales of roughness, mimicking natural water-repellent materials, such as the lotus leaf [28], that are known to derive their high performance from their hierarchical geometry. Hierarchical yet irregular geometries have been achieved in other ways, including by gold-assisted electroless etching of silicon to create a multi-scale porous surface with overhanging features and a static water contact angle exceeding 160° [29].

Another potentially scalable approach to creating re-entrant structures is to deposit particles or fibers on to the target substrate, by spraying, painting, or dip-coating. For example, Campos sprayed precipitated silica nanoparticles in a fluoropolymer binder [30], Tarwal employed pyrolytic formation of ZnO from a heated, sprayed zinc acetate solution [31], Zhang smeared a polymer chalk of polydivinylbenzene on to a set of target surfaces [32], and Lu sprayed titania nanoparticles on to target substrates [33]. Electrospinning has also been widely employed (e.g. [34]). In all of these cases a porous surface with re-entrant microscopic geometries is created. Additionally, dip-coating of woven meshes with fluoropolymer solutions has been shown to be an effective way of combining a controlled re-entrant structure with a liquid-repellent surface chemistry [3].

Irregular, reentrant-featured surfaces certainly promise to be much less expensive to produce than regular, lithographically defined ones, and can be scaled more readily to larger areas [17], but their distributions of surface feature geometries—and thus their performance—are more challenging to characterize. The behavior of a liquid on a textured surface has conventionally been modeled either as completely wetting the surface (Wenzel mode [35], figure 1(a)) or as sitting entirely on top of the surface and not penetrating any pores (Cassie–Baxter mode [4], figure 1(b)). This binary distinction cannot, however, represent the true behavior of the many types of surfaces whose textures are spatially heterogeneous, having, for example, pores with a range of wall angles. In these situations, some pores may wet while others remain empty, depending on their local geometries.

Here, therefore, we introduce a new model to characterize geometrically heterogeneous surfaces accurately. Our model takes account of the average wall angle of surface structures as well as the degree of variability of wall angle and the average roughness of the structures. The new model's crucial contribution is the introduction of a parameter that captures the variability of pore geometry. It thus goes beyond the derivations [36–39] and modifications [40, 41] that have previously been used to specialize the Cassie–Baxter model for particular regular geometries such as woven meshes. All of these previously proposed models are entirely deterministic and regard a surface as being capable of being defined by a small set of fixed dimensional parameters. In contrast, the approach that we describe here incorporates pore-to-pore variation and relates a liquid's apparent contact angle to the particular *fraction* of pores that are filled at a given time.

Modeling framework

We model a surface as having many equal-volume pores with sidewalls whose re-entrant angles Ψ near their tips approximately follow a Gaussian distribution with mean Ψ_0 and standard deviation σ_0 (figure 1(c)). Let $P(\Psi)$ be the cumulative distribution function for Ψ:

$$P(\Psi) \approx \int_{-\infty}^{\Psi} \frac{1}{\sigma_0\sqrt{2\pi}} e^{-\left(\frac{(\Psi'-\Psi_0)^2}{2\sigma_0^2}\right)} d\Psi'. \quad (1)$$

In our model, a pore will instantaneously and completely fill when θ_0, the contact angle of the liquid on a flat surface, is less than the re-entrant angle: $\theta_0 < \Psi$. In that situation, the surface tension of the liquid will pull the liquid down into the pore until it fills. Conversely, we assume that a pore remains completely empty when $\theta_0 \geqslant \Psi$ and the surface tension holds the liquid out of the pore. We assume that a liquid droplet making contact with the surface is large enough to encounter many pores. Below the droplet, the proportion of pores filled, ϕ_F, for a given value of θ_0 is:

$$\phi_F = 1 - P(\theta_0). \quad (2)$$

We then model the overall apparent contact angle, θ^*, of a droplet of liquid on the surface structure using a generalized Cassie–Baxter model [4]. The general Cassie–Baxter model expresses the cosine of the apparent contact angle on a composite surface as the area-weighted sum of the contact angle cosines for each of the components, *i*, of the surface:

$$\cos\theta^* = \sum_i f_i r_i \cos\theta_{0,i}, \tag{3}$$

where f_i is the fraction of the surface's projected area that is occupied by component i, r_i is the *roughness* of the component (i.e. the ratio of total surface area to projected area) and $\theta_{0,i}$ is the contact angle of the liquid on a flat surface with the same surface chemistry as component i.

Our specific model assumes that the projected surface area of the porous film is divided into three components (figure 1(c)). Firstly, a fraction ϕ_T of the area sits at the tips of the material between the pores and is always in contact with the liquid. The remaining area, the fraction $(1 - \phi_T)$, is divided between a proportion ϕ_F of pores that are filled, and a proportion $(1 - \phi_F)$ of unfilled pores in which a liquid–air interface exists. The pores are assumed to have a roughness r such that the total surface area of a pore is r times the projected area of one pore opening. This roughness plays a role only when a pore is filled with liquid. The general Cassie–Baxter model thus reduces to:

$$\cos\theta^* = \phi_T \cos\theta_0 + (1 - \phi_T)[\phi_F\, r \cos\theta_0 - (1 - \phi_F)]. \tag{4}$$

Equation (4) encapsulates the essential contribution of our new model: that the apparent contact angle of a liquid on a surface with a range of pore geometries can be written as a function of the *fraction* of pores, ϕ_F, filled by a given liquid. That fraction is, in turn, a function of the distribution of pore angles, as expressed in equation (1), and the contact angle θ_0 of the liquid on a flat surface (equation (2)).

When a pore is not filled with liquid, the local effective contact angle is taken to be 180°, since in the complete absence of any solid surface, a volume of liquid naturally forms a sphere. Thus, the second term inside the square brackets of equation (4), corresponding to unfilled pores, is $-(1 - \phi_F)$, since the cosine of the contact angle for the liquid–air interface is -1. In cases where equation (4) would imply that $\cos\theta^* > 1$, $\cos\theta^*$ is set to equal 1 and complete wetting is assumed to take place. By measuring the apparent contact angles, θ^*, of four or more liquids with a range of surface tensions, we can fit estimates for Ψ_0, σ_0, ϕ_T and r, and thereby characterize a surface.

The assumption of a Gaussian distribution of the angle Ψ is approximate because in engineered surfaces Ψ is usually constrained to lie between –90° and 180°; Ψ cannot, in reality, extend towards $\pm\infty$ as a Gaussian distribution would imply. Nevertheless, for the values of Ψ_0 and σ_0 that we fit for actual surfaces, a negligible portion of the tails of a Gaussian distribution lie outside a realistic range of Ψ.

Methods

To demonstrate the model's ability to describe the behavior of real surfaces, we have fabricated and characterized three porous, liquid-repellant coatings. All materials for fabricating and characterizing these coatings were obtained from Sigma-Aldrich.

The first test coating was a nanoporous zinc oxide that was grown hydrothermally on to aluminum. The porous zinc oxide surfaces were synthesized by immersing an aluminum scanning electron microscopy (SEM) sample-mounting peg into a 25 mM equimolar aqueous solution of zinc nitrate and hexamine at 70 °C for 90 min. The ZnO-coated substrates were then oxygen plasma-treated (60 W, 200 mTorr, 2 min) to clean them and impart hydroxyl surface termination.

The zinc oxide surfaces were modified in one of three ways to impart hydrophobic surface chemistry. In the first modification, the substrate was placed, immediately after plasma treatment, in a vacuum desiccator with 100 μl of 1H, 1H, 2H, 2H-Perfluorooctyltrichlorosilane (PFOS). The desiccator was then pumped for 20 min to vaporize the silane followed by letting it settle for 40 min before venting the chamber. Upon removal, the substrates were rinsed with deionized water to remove unreacted perfluorosilane, dried, and finally annealed at 120 °C for 1 h on a hot plate. In the second modification, the substrate was dipped in a 3% perfluorooctyl polyhedral oligomeric silsesquioxane (PFO-POSS) solution in Vertrel™ XF (Dupont) for 3 min and then used as coated. In the third modification, the substrate was dipped in 1% (3-aminopropyl)triethoxysilane (APTES) solution in deionized water for 10 min, and then rinsed with deionized water and heated to 120 °C on a hot plate for 1 h.

As a second test-case for the model, a film composed of approximately 600 nm diameter polyvinylidene fluoride (PVDF) spheres was synthesized by spinodal decomposition from a ternary solvent system. A 20 wt% polymer solution was created by dissolving PVDF pellets into dimethylformamide in an 80 °C water bath for 3 h. 1.7 wt% deionized water was then loaded into the solution. The solution was vortex-mixed for 5 min; then 50.0 μl of the solution was drop-cast on to an aluminum SEM peg, and spun at 1200 rpm for 30 s. Directly after spinning, the sample was submerged in deionized water at 90 °C for 30 min. After removal, the sample was air-dried then pumped under dynamic vacuum at room temperature overnight to ensure that the pores were free of solvent and water.

As a third test-case, a porous polytetrafluoroethylene (PTFE) film was created via templating with sacrificial poly(styrene-co-divinylbenzene) (PS) microspheres, according to the procedure of van der Wal [42]. Briefly, PTFE and PS colloid suspensions in water were mixed to give a solid volume fraction of 60%, with 67% of the solid volume being the sacrificial PS. 100 μl of this suspension was blade-cast on to an aluminum SEM peg and placed on a hot plate at 120 °C for 1 h to evaporate the water. A further hot-plate treatment at 290 °C for 30 min was used to sinter the PTFE particles together and partially decompose the sacrificial PS. The PS was then removed by washing in acetone.

We have used six probe liquids to characterize these surfaces; these are, in descending order of surface tension, water (73 mN m^{-1} [43]), glycerol (64 mN m^{-1} [43]), thiodiglycol (54 mN m^{-1} [43]), polyethylene glycol diacrylate with a molar mass of 700 g (~43 mN m^{-1} [44]), dipropylene glycol (34 mN m^{-1} [43]), and methanol (23 mN m^{-1} [43]). Sessile contact angle measurements were made by pipetting 5 μl of the liquid on to the surface, and then, after waiting for approximately 15 s, imaging the droplet from the side using a 4X objective (Olympus Plan Achromat), a 30 mm focal-length achromatic doublet (Thorlabs, Newton, NJ), and a 1280 × 1024-pixel CMOS image sensor (Thorlabs, model DCC1645C). Images were analyzed to extract contact angles using ImageJ [45] with the low-bond asymmetric drop shape analysis algorithm described by Stalder [46, 47]. Each material/probe liquid combination was measured with five separate droplets.

Values of θ_0 for each liquid–solid pairing were determined by directly measuring the liquid's contact angle on a flat silicon wafer treated with the same surface termination as the textured surface. Then, contact angles between the probe liquids and the textured surfaces were measured. Each liquid–solid pairing was characterized with five separate contact angle measurements made using different droplets.

For each model calibration, an upper bound for ϕ_T is estimated by considering θ^* for the highest-surface-tension liquid tested—in this case water—and assuming that no pores are filled in that case. For the ZnO surfaces, an upper bound on ϕ_T was computed using the results for the PFO-POSS termination, the least-wetting treatment. Equation (4) then reduces and rearranges to:

$$\phi_T \approx \frac{\cos\theta^* + 1}{\cos\theta_0 + 1}. \tag{5}$$

This value of ϕ_T is an upper bound because it is possible that a few pores are in fact filled with water during the observation of θ^*, so that not all the liquid–solid contact area is located within the tips of the structure. By using our physical understanding of the liquid–solid interaction to establish an upper bound on ϕ_T prior to the fitting procedure, we eliminate the possibility of extracting an unrealistically high value for ϕ_T during fitting. This approach helps to increase confidence in the values that are extracted for all four model parameters. With θ_0 and the upper bound on ϕ_T established, a least-squares error minimization routine (Microsoft Excel's Solver plug-in with the generalized reduced gradient algorithm) is then used to fit Ψ_0, σ_0, ϕ_T and r.

Results

Table 1 records the means and standard errors of the contact angles measured across all five surfaces and six probe liquids. As shown in figure 2(a), the zinc oxide pore morphology is highly irregular, and pores are surrounded by thin walls of material that are aligned approximately perpendicularly to the surface of the sample but with considerable angular variation. Figure 2(b) shows that a single set of geometrical parameters fits the data closely for all six probe liquids and all three surface terminations. Our model finds that pores are, on average, moderately re-entrant, with $\Psi_0 = 51°$, and with a broad spread of pore geometry: $\sigma_0 = 25°$ (table 2). The gradual increase of cos θ^* with cos θ_0 indicates that a progressively larger proportion of the pores becomes filled as the contact angle of the probe liquid on a smooth surface reduces (i.e. as cos θ_0 increases).

In figure 3, we re-plot the contact angle data from the ZnO with PFOS surface termination, together with results for the PVDF and PTFE surfaces. These three surfaces show quite different relationships between cos θ^* and cos θ_0. The PVDF surface exhibits a much sharper non-wetting-to-wetting transition than we observe with the zinc oxide. From our contact angle measurements, we extract for the PVDF an effective average sidewall angle of $\Psi_0 = 57°$ and a low pore sidewall angle variability of $\sigma_0 = 1°$ (table 2). This apparent tight distribution could be explained by the reasonably uniform distribution of PVDF sphere diameter (figure 4(a)) that results from the precipitation kinetics. The curvatures locally encountered by a liquid droplet at its interface with the solid are likely to be spatially uniform, even though the pores within the film are irregular in shape. On the other hand, a high within-pore roughness, r, of 11.2 is fit, and we attribute this result both to the micro-scale roughness created by the irregular clustering of microspheres and to the nano-scale surface texture of individual microspheres that is seen in a higher-magnification electron micrograph of the material (figure 4(b)).

The PTFE structure, meanwhile, contains a broad distribution of pore sizes (figure 4(c)) by virtue of the wide distribution of sacrificial PS sphere diameters used: we estimate that these diameters range from 1 to 10 μm. We

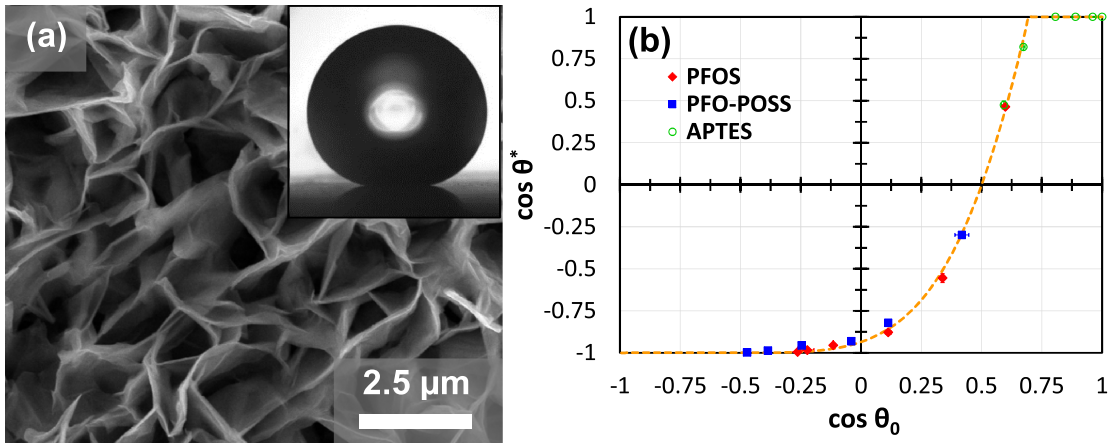

Figure 2. Calibration of the surface wettability model for zinc oxide nanoporous surfaces terminated with PFOS, PFO-POSS and APTES. The pores in the hydrothermally grown ZnO have highly heterogeneous sizes and sidewall angles, as shown in a scanning electron micrograph (a). Inset: 5 μl droplet (diameter $\approx$ 2.1 mm) on the surface. A single set of fit parameters accurately describes the dependence of cos θ^* on cos θ_0 for this surface geometry with all three surface terminations (b). Error bars correspond to $\pm$ one standard error of the mean, based on five measurements. In many cases, error bars are smaller than symbols. Probe liquids are detailed in the results section. On a given surface, the higher the liquid's surface tension, the lower the value of cos θ_0. The model fit is shown as a dashed line.

Table 1. Measured apparent contact angles (in degrees) for the five surfaces and six probe liquids tested. The mean of five separate droplet measurements and the standard error of the mean are shown. Where the contact angle is recorded as '<10', the surface was observed to wet completely, and contact angles were thus not measured.

	Surface material									
	PFOS–ZnO		POSS–ZnO		APTES–ZnO		PTFE		PVDF	
Probe liquid	Mean	Std. err.	Mean	Std. err.	Mean	Std. err.	Mean	Std. err.	Mean	Std. err.
Apparent contact angles on textured surfaces (θ^*)										
Water	173.8	0.8	175.8	0.6	61.6	1.5	163.3	0.6	169.2	0.9
Glycerol	169.6	0.5	170.8	0.4	34.8	1.9	158.1	0.7	169.0	0.9
Thiodiglycol	162.7	0.6	163.1	0.8	<10	—	152.8	0.4	<10	—
Polyethylene glycol diacrylate	151.5	1.5	158.6	0.3	<10	—	147.3	1.0	<10	—
Dipropylene glycol	123.7	0.8	145.2	0.5	<10	—	137.2	1.6	<10	—
Methanol	62.3	1.7	107.4	0.9	<10	—	108.5	1.4	<10	—
Contact angles on smooth surfaces (θ_0)										
Water	105.3	0.2	118.2	0.3	53.7	0.7	122.6	1.3	79.0	2.0
Glycerol	102.9	1.6	112.7	0.7	47.7	0.5	114.6	1.0	65.9	0.6
Thiodiglycol	96.6	0.5	104.3	0.4	36.2	1.1	107.2	0.4	57.8	1.0
Polyethylene glycol diacrylate	83.5	0.7	92.3	0.6	27.1	1.4	96.5	0.3	35.0	1.1
Dipropylene glycol	70.2	1.0	83.5	0.7	16.0	2.5	90.8	0.6	18.7	0.5
Methanol	53.2	0.8	65.2	1.8	<10	—	65.4	1.5	20.2	1.1

Table 2. Summary of the model parameters fit for three heterogeneous, nanoporous surfaces and for one regular, lithographically-produced surface. The fitting parameters are: mean reentrant angle (Ψ_0), standard deviation of the reentrant angle (σ_0), within-pore surface roughness factor (r), and top-of-surface solid fraction (ϕ_T).

Surface	Ψ_0	σ_0	r	ϕ_T
Porous ZnO	51°	25°	3.5	0.0051
PVDF microspheres	57°	1°	11.2	0.014
PTFE templated by sacrificial PS microspheres (using the method of van der Wal [42])	54°	38°	1.4	0.092
Regular, reentrant disk array [5]	27°	0°	1.2	0.051

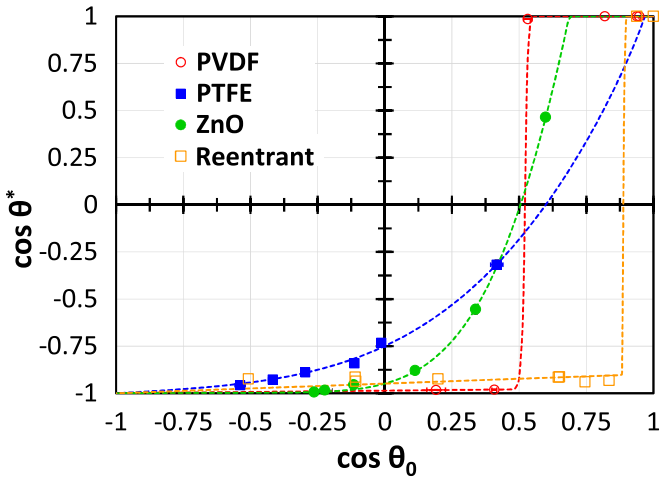

Figure 3. Calibration of the surface wettability model for PVDF microsphere foams, porous PTFE templated with sacrificial PS microspheres, hydrothermally grown nanoporous ZnO terminated with PFOS, and a regular reentrant SiO_2/Si microstructure reported by Liu [5]. The model calibrations indicate that the PTFE film shows the most gradual increase of cos $\boldsymbol{\theta}^*$ with cos $\boldsymbol{\theta}_0$, consistent with a large spatial variation of pore geometry. Symbols for PTFE, PVDF and ZnO represent the mean of five measurements and error bars represent $\pm$ one standard error of the mean, based on the five measurements (in most cases, error bars are smaller than the symbols). The symbols labeled 'reentrant' are the results of Liu and represent one measurement per data point. Dashed lines show the corresponding model fits.

extract surface characteristics of $\Psi_0 = 54°$ and $\sigma_0 = 38°$, making this appear to be the most geometrically heterogeneous of the surfaces we have examined.

Discussion

We have used our statistical model to extract three very different wettability characteristics from the three porous surfaces. None of these trends could have been captured with a simple model of completely regular, straight-sidewalled features; such a model can comprehend only a single, critical value of cos θ_0 below which the surface is assumed to be in Cassie–Baxter mode, and above which pore wetting is assumed to occur spontaneously and completely.

It is conceivable that the observed shapes of the cos θ^* versus cos θ_0 plots could be reproduced without considering pore-to-pore variability by developing instead a tailored geometrical model for sidewall profile whose angle varied with depth in such a way that every single pore would progressively fill at the same rate as cos θ_0 increased. However, a very particular profile would need to be proposed for each and every material characterized, in order to capture fully the various transitions from completely non-wetting to completely wetting behavior that are shown in figures 2 and 3. Our model of pore angle variability, with only four fitting parameters, is a much more realistic and versatile way to explain how irregular surfaces wet.

To contrast our randomly distributed surface geometries with a more regular geometry, we have used the new model to interpret previously published data from a highly regular array of singly reentrant surface structures that was produced lithographically by Liu and Kim [5]. These structures consist of a square array of silicon oxide disks of diameter ~20 μm that are supported by narrower silicon pillars and coated with ~150 nm of C_4F_8 hydrophobic polymer. As expected, this surface exhibits a far sharper transition from non-wetting to wetting as cos θ_0 increases (figure 3) than do our three more variable porous surfaces. Our least-squares fitting procedure extracts an average re-entrant angle of $\Psi_0 = 27°$—which is plausible if the etching of the silicon oxide disks involves some sidewall tapering—together with zero angle variability σ_0, which is consistent with highly repeatable lithographic production. For this particular surface, therefore, it is reasonable to suppose that the inter-disk regions are either completely empty or completely filled according to the liquid used. Consequently, while our model-fitting procedure extracts a roughness value between the structures of $r = 1.2$, this value has no practical relevance because as soon as any inter-structure void fills, wetting is complete and cos θ^* becomes 1.

We have thus shown that our model can be used to characterize the relationship between a liquid's contact angle on a flat surface and its apparent contact angle on a range of porous or otherwise randomly distributed material geometries. The model predicts a one-to-one relationship between the contact angle on a flat surface, θ_0, and the apparent contact angle. It does not capture the possible effects of 'breakthrough', where a load—such as a droplet's Laplace pressure or a randomly occurring inertial force—causes the liquid surface to deform into the pore, touch its base, and wet the geometry. Rather, our model assumes that as cos θ_0 increases, the *sidewalls*

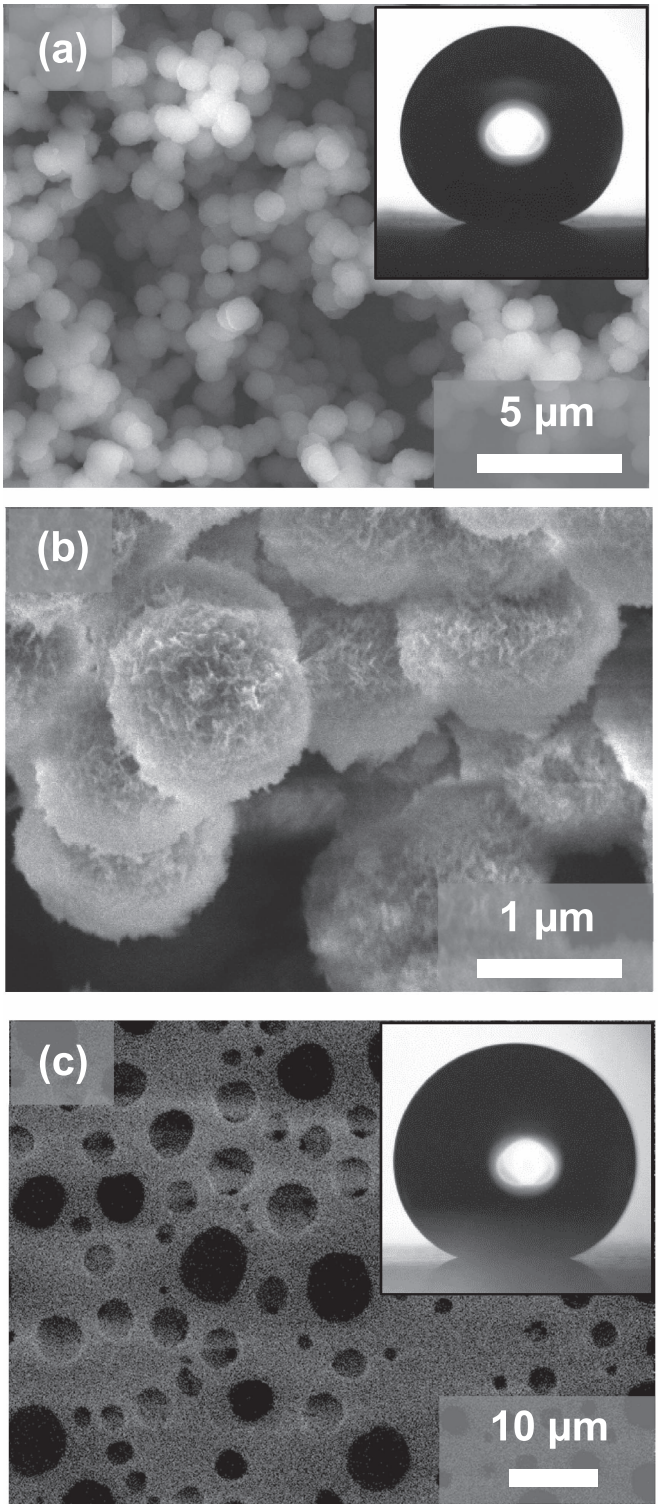

Figure 4. Scanning electron micrographs of the PVDF foam shows microspheres with uniformly distributed diameters (a) and nanoscale surface roughness (b). The PTFE film exhibits large variation of pore size (c). Insets in (a) and (c) show 5 μl droplets (diameter $\approx$ 2.1 mm) on the respective surfaces.

of the pores progressively guide liquid into an increasing fraction of the pores, so that the increase in cos θ^* with cos θ_0 is gradual and predictable, and relies only on the action of the liquid's surface tension within the pores.

For the ZnO, PVDF and PTFE surfaces that we have demonstrated here, our model is accurate because the pores are mostly sub-micrometer in size and thus highly robust against breakthrough. According to the model of, for example, Chhatre *et al* [3], we estimate our surfaces' robustness—essentially, the ratio of required breakthrough pressure to a typical droplet's Laplace pressure—to be around 1000. In other words, it is very unlikely that a spontaneous Cassie–Baxter-to-Wenzel transition occurs in these structures. For materials with

considerably larger pores, it may become necessary to incorporate robustness as an additional factor. Additionally, our model does not consider contact angle hysteresis or the relationship between pore geometry and pinning. Both of these considerations may be relevant in some applications, particularly those involving condensation of the liquid that is to be repelled.

Concluding remarks

We have demonstrated a new approach to modeling the dependence of a liquid's apparent contact angle on the geometrical characteristics of a porous surface on which it sits. Our model is simple to calibrate, requiring only contact-angle measurements to be made, and provides a framework for experimentally quantifying the variability of pore geometries on surfaces. We have demonstrated the calibration procedure for three geometrically heterogeneous porous surfaces that we have produced, as well as for one previously reported, spatially regular structure. These four materials show considerable differences between wetting characteristics that can be explained by considering pore geometry variation. All three of our coating methods involve inexpensive reagents and simple apparatus, and thus promise to be more affordable than precisely engineered, geometrically regular, patterned surfaces. The coatings can be applied to non-flat surfaces without special handling.

In addition to providing new insight into the importance and role of pore shape variability on droplet contact angles, our modeling technique offers a rapid way to screen candidate surface deposition and synthesis processes. One of the method's key strengths is that once a particular surface geometry (e.g. that of porous zinc oxide) has been characterized, the cos θ_0 versus cos θ^* relationship can be used to predict the effect of modifying the surface chemistry (e.g. PFOS or APTES) applied to that geometry, provided that the surface modification does not alter the geometry. Thus, our approach could readily be applied to the screening of multiple candidate liquid-repellent coating processes to quantify their performance.

Acknowledgments

The authors gratefully acknowledge the assistance of Paul Lum and the staff of the Biomolecular Nanotechnology Center at UC Berkeley. This research was supported by the National Research Foundation, Prime Minister's Office, Singapore, as part of the Singapore–Berkeley Building Efficiency and Sustainability in the Tropics program.

References

[1] Tuteja A, Choi W, Ma M, Mabry J M, Mazzella S A, Rutledge G C, McKinley G H and Cohen R E 2007 Designing superoleophobic surfaces *Science* **318** 1618–22
[2] Tuteja A, Choi W, Mabry J M, McKinley G H and Cohen R E 2008 Robust omniphobic surfaces *Proc. Natl Acad. Sci.* **105** 18200–5
[3] Chhatre S S, Choi W, Tuteja A, (Kenneth) Park K-C, Mabry J M, McKinley G H and Cohen R E 2010 Scale dependence of omniphobic mesh surfaces *Langmuir* **26** 4027–35
[4] Cassie A B D and Baxter S 1944 Wettability of porous surfaces *Trans. Faraday Soc.* **40** 546–51
[5] Liu T 'L' and Kim C-J 'C J' 2014 Turning a surface superrepellent even to completely wetting liquids *Science* **346** 1096–100
[6] Xue C-H, Jia S-T, Zhang J and Ma J-Z 2010 Large-area fabrication of superhydrophobic surfaces for practical applications: an overview *Sci. Technol. Adv. Mater.* **11** 33002
[7] Chen S, Li X, Li Y and Sun J 2015 Intumescent flame-retardant and self-healing superhydrophobic coatings on cotton fabric *ACS Nano* **9** 4070–6
[8] Zhou H, Wang H, Niu H, Gestos A and Lin T 2013 Robust, self-healing superamphiphobic fabrics prepared by two-step coating of fluoro-containing polymer, fluoroalkyl silane, and modified silica nanoparticles *Adv. Funct. Mater.* **23** 1664–70
[9] Teisala H, Tuominen M and Kuusipalo J 2014 Superhydrophobic coatings on cellulose-based materials: fabrication, properties, and applications *Adv. Mater. Interfaces* **1** n/a-n/a
[10] Smith J D, Dhiman R, Anand S, Reza-Garduno E, Cohen R E, McKinley G H and Varanasi K K 2013 Droplet mobility on lubricant-impregnated surfaces *Soft Matter* **9** 1772–80
[11] Li J, Shi L, Chen Y, Zhang Y, Guo Z, Su B and Liu W 2012 Stable superhydrophobic coatings from thiol-ligand nanocrystals and their application in oil/water separation *J. Mater. Chem.* **22** 9774
[12] Cao L, Jones A K, Sikka V K, Wu J and Gao D 2009 Anti-icing superhydrophobic coatings *Langmuir* **25** 12444–8
[13] Kim P, Wong T-S, Alvarenga J, Kreder M J, Adorno-Martinez W E and Aizenberg J 2012 Liquid-infused nanostructured surfaces with extreme anti-ice and anti-frost performance *ACS Nano* **6** 6569–77
[14] McHale G, Shirtcliffe N J, Evans C R and Newton M I 2009 Terminal velocity and drag reduction measurements on superhydrophobic spheres *Appl. Phys. Lett.* **94** 64104
[15] Mann E E, Manna D, Mettetal M R, May R M, Dannemiller E M, Chung K K, Brennan A B and Reddy S T 2014 Surface micropattern limits bacterial contamination *Antimicrob. Resist. Infect. Control* **3** 28
[16] 'Sharklet Technologies.' [Online]. Available: www.sharklet.com (Accessed:14-July-2016)
[17] Miljkovic N and Wang E N 2013 Condensation heat transfer on superhydrophobic surfaces *MRS Bull.* **38** 397–406
[18] Miljkovic N, Enright R, Nam Y, Lopez K, Dou N, Sack J and Wang E N 2013 Jumping-droplet-enhanced condensation on scalable superhydrophobic nanostructured surfaces *Nano Lett.* **13** 179–87

[19] Varanasi K K, Hsu M, Bhate N, Yang W and Deng T 2009 Spatial control in the heterogeneous nucleation of water *Appl. Phys. Lett.* **95** 94101
[20] Casanova F, Chiang C E, Li C-P, Roshchin I V, Ruminski A M, Sailor M J and Schuller I K 2008 Gas adsorption and capillary condensation in nanoporous alumina films *Nanotechnology* **19** 315709
[21] Lee W, Park B G, Kim D H, Ahn D J, Park Y, Lee S H and Lee K B 2010 Nanostructure-dependent water-droplet adhesiveness change in superhydrophobic anodic aluminum oxide surfaces: from highly adhesive to self-cleanable *Langmuir* **26** 1412–5
[22] Masuda H, Yada K and Osaka A 1998 Self-ordering of cell configuration of anodic porous alumina with large-size pores in phosphoric acid solution *Japan. J. Appl. Phys.* **37** L1340–2
[23] Li M, Zhai J, Liu H, Song Y, Jiang L and Zhu D 2003 Electrochemical deposition of conductive superhydrophobic zinc oxide thin films *J. Phys. Chem.* B **107** 9954–7
[24] Yin S and Sato T 2005 Mild solution synthesis of zinc oxide films with superhydrophobicity and superhydrophilicity *J. Mater. Chem.* **15** 4584
[25] Wang Z L 2004 Zinc oxide nanostructures: growth, properties and applications *J. Phys.: Condens. Matter* **16** R829
[26] Hosono E, Fujihara S, Honma I and Zhou H 2005 Superhydrophobic perpendicular nanopin film by the bottom-up process *J. Am. Chem. Soc.* **127** 13458–9
[27] Wang C-F, Tzeng F-S, Chen H-G and Chang C-J 2012 Ultraviolet-durable superhydrophobic zinc oxide-coated mesh films for surface and underwater–oil capture and transportation *Langmuir* **28** 10015–9
[28] Koch K, Bhushan B, Jung Y C and Barthlott W 2009 Fabrication of artificial Lotus leaves and significance of hierarchical structure for superhydrophobicity and low adhesion *Soft Matter* **5** 1386
[29] Cao L, Price T P, Weiss M and Gao D 2008 Super water- and oil-repellent surfaces on intrinsically hydrophilic and oleophilic porous silicon films *Langmuir* **24** 1640–3
[30] Campos R, Guenthner A J, Meuler A J, Tuteja A, Cohen R E, McKinley G H, Haddad T S and Mabry J M 2012 Superoleophobic surfaces through control of sprayed-on stochastic topography *Langmuir* **28** 9834–41
[31] Tarwal N L and Patil P S 2010 Superhydrophobic and transparent ZnO thin films synthesized by spray pyrolysis technique *Appl. Surf. Sci.* **256** 7451–6
[32] Zhang Y-L, Wang J-N, He Y, He Y, Xu B-B, Wei S and Xiao F-S 2011 Solvothermal synthesis of nanoporous polymer chalk for painting superhydrophobic surfaces *Langmuir* **27** 12585–90
[33] Lu Y, Sathasivam S, Song J, Crick C R, Carmalt C J and Parkin I P 2015 Robust self-cleaning surfaces that function when exposed to either air or oil *Science* **347** 1132–5
[34] Ding B, Ogawa T, Kim J, Fujimoto K and Shiratori S 2008 Fabrication of a super-hydrophobic nanofibrous zinc oxide film surface by electrospinning *Thin Solid Films* **516** 2495–501
[35] Wenzel R N 1936 Resistance of solid surfaces to wetting by water *Ind. Eng. Chem.* **28** 988–94
[36] Whyman G, Bormashenko E and Stein T 2008 The rigorous derivation of Young, Cassie–Baxter and Wenzel equations and the analysis of the contact angle hysteresis phenomenon *Chem. Phys. Lett.* **450** 355–9
[37] Nosonovsky M 2007 Multiscale roughness and stability of superhydrophobic biomimetic interfaces *Langmuir* **23** 3157–61
[38] McHale G 2007 Cassie and Wenzel: were they really so wrong? *Langmuir* **23** 8200–5
[39] Marmur A 2003 Wetting on hydrophobic rough surfaces: to be heterogeneous or not to be? *Langmuir* **19** 8343–8
[40] Erbil H Y and Cansoy C E 2009 Range of applicability of the Wenzel and Cassie−Baxter equations for superhydrophobic surfaces *Langmuir* **25** 14135–45
[41] Choi W, Tuteja A, Mabry J M, Cohen R E and McKinley G H 2009 A modified Cassie–Baxter relationship to explain contact angle hysteresis and anisotropy on non-wetting textured surfaces *J. Colloid Interface Sci.* **339** 208–16
[42] van der Wal P and Steiner U 2007 Super-hydrophobic surfaces made from Teflon *Soft Matter* **3** 426–9
[43] 'Surface tension values of some common test liquids for surface energy analysis.' [Online]. Available: http://surface-tension.de/ (Accessed: 27-September-2016)
[44] Suh K Y and Langer R 2003 Microstructures of poly (ethylene glycol) by molding and dewetting *Appl. Phys. Lett.* **83** 1668–70
[45] 'ImageJ.' [Online]. Available: https://imagej.nih.gov/ij/ (Accessed: 11-July-2016)
[46] Stalder A F, Melchior T, Müller M, Sage D, Blu T and Unser M 2010 Low-bond axisymmetric drop shape analysis for surface tension and contact angle measurements of sessile drops *Colloids Surf. Physicochem. Eng. Asp.* **364** 72–81
[47] 'Drop Analysis.' [Online]. Available: http://bigwww.epfl.ch/demo/dropanalysis/ (Accessed: 11-July-2016)